

Development of a single-cell X-ray fluorescence flow cytometer

Andrew M. Crawford,^a Patrick Kurecka,^a Tsz Kwan Yim,^a Claire Kozemchak,^a Aniruddha Deb,^{a,b} Lubomír Dostál,^a Cheng-Jun Sun,^c Dale L. Brewé,^c Raul Barrea^d and James E. Penner-Hahn^{a,b*}

Received 23 October 2015

Accepted 17 May 2016

Edited by P. A. Pianetta, SLAC National Accelerator Laboratory, USA

Keywords: flow cytometry; X-ray fluorescence; single cell; metallome; homeostasis.

Supporting information: this article has supporting information at journals.iucr.org/s

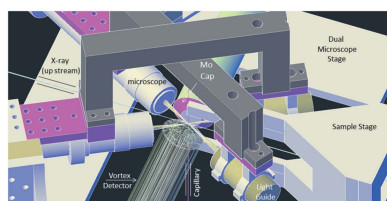
^aDepartment of Chemistry, University of Michigan, Ann Arbor, MI 48109-1055, USA, ^bDepartment of Biophysics, University of Michigan, Ann Arbor, MI 48109-1055, USA, ^cX-ray Science Division, Argonne National Laboratory, 9700 South Cass Avenue, Argonne, IL 60439, USA, and ^dDepartment of Physics, DePaul University, Chicago, IL 60604, USA. *Correspondence e-mail: jeph@umich.edu

An X-ray fluorescence flow cytometer that can determine the total metal content of single cells has been developed. Capillary action or pressure was used to load cells into hydrophilic or hydrophobic capillaries, respectively. Once loaded, the cells were transported at a fixed vertical velocity past a focused X-ray beam. X-ray fluorescence was then used to determine the mass of metal in each cell. By making single-cell measurements, the population heterogeneity for metals in the μM to mM concentration range on fL sample volumes can be directly measured, a measurement that is difficult using most analytical methods. This approach has been used to determine the metal composition of 936 individual bovine red blood cells (bRBC), 31 individual 3T3 mouse fibroblasts (NIH3T3) and 18 *Saccharomyces cerevisiae* (yeast) cells with an average measurement frequency of ~ 4 cells min^{-1} . These data show evidence for surprisingly broad metal distributions. Details of the device design, data analysis and opportunities for further sensitivity improvement are described.

1. Introduction

In addition to their organic constituents, cells contain a variety of bulk, trace and ultra-trace elements. In most cases, cells appear to have homeostatic mechanisms that maintain elemental concentrations within narrow limits. Knowledge of these cellular concentrations under different conditions is important for understanding homeostasis. Relevant concentrations range from ~ 10 – 100 mM for bulk elements (*e.g.* P, K, Na and Fe in red blood cells) to 100 μM – 3 mM for trace elements (*e.g.* Zn, Mg, Ca and Fe in other cell types) to 1 – 20 μM for ultra-trace elements (Cu, Ni, Mn, Se) (Herring *et al.*, 1960*a*; Shamberger, 2003). These concentrations are perturbed under various conditions and disease states (Herring *et al.*, 1960*b*; Kakkar & Makkar, 2009), and these variations can be clinically diagnostic. For example, patients with spherocytosis have red blood cells with higher than normal Fe content in relation to their volume (Kakkar & Makkar, 2009).

Toxic metals can also result in disruption of metal concentrations. For example, cadmium has been found to biologically mimic the substrate binding of zinc (Kamizono *et al.*, 1989). This is in part why Cd is toxic, because although it can replace Zn^{2+} structurally it cannot replace it functionally (Hartwig, 2001). Likewise, dietary or genetic disruption of metal ion homeostasis, particularly copper and iron, causes many disease states (Fahrni, 2007; Madsen & Gitlin, 2007).



© 2016 International Union of Crystallography

Homeostatic mechanisms governing the so-called ‘metallome’ are interconnected and a change in one regulatory process can impact others (Ariño *et al.*, 2010; Bertinato & L’Abbe, 2004; Chillappagari *et al.*, 2010; Dann *et al.*, 2007; Dlouhy & Outten, 2013; Eide, 2009; Zhao *et al.*, 1998). For example, increases in intracellular Zn in *S. cerevisiae* have been attributed to increased expression of Fet4, which transports Cu, Fe and Zn (Li & Kaplan, 1998; Pagani *et al.*, 2007). As such, characterization of the complete metallome is very important.

Finally, dynamic regulatory processes involved in homeostasis can lead to significant heterogeneity in elemental concentrations across a population of cells (Davey & Kell, 1996; Kalisky & Quake, 2011; Musat *et al.*, 2008; Leslie, 2011; Eide, 2009; Brehm-Stecher & Johnson, 2004). For all these reasons, a complete characterization of metal homeostasis requires not only the mean concentration of an element for a sample but also the cell-to-cell variability in concentrations in order to truly understand homeostatic responses of the metallome. As such, there is a pressing need for high-throughput techniques capable of elemental analysis of single cells.

There are several methods that have sufficient sensitivity to give single-cell elemental compositions. These include mass spectrometry (MS), metal-specific organic fluorophores, and intrinsic (X-ray) fluorescence (McRae *et al.*, 2009; Penner-Hahn, 2014). Fluorescent probes have been used to report on subcellular transition metal cations such as Zn (Kikuchi *et al.*, 2004) or Cu (Yang *et al.*, 2005) and can have excellent sensitivity. However, these are generally less useful for paramagnetic ions, and even for diamagnetic metals fluorescent probes are limited to detecting only the chelatable metal in the cell. Moreover, by binding to metals in the cell, fluorophores can disrupt metal homeostasis. MS methods can have exquisite sensitivity and multielement detection capability. Recent work has demonstrated the ability of inductively coupled plasma to ionize the metals from single cells (Miyashita *et al.*, 2014; Mueller *et al.*, 2014; Ho & Chan, 2010). Using quadrupole MS detection (Groombridge *et al.*, 2013) it was possible to detect as few as $\sim 10^5$ Mg atoms per cell; simultaneous multi-element detection is possible using time-of-flight MS, although at lower sensitivity. The challenges of MS methods for single-cell analysis include incomplete cell vaporization, incomplete metal ionization, and the variability in ionization efficiency for different elements (so-called matrix effects). In contrast to these methods, X-ray fluorescence (XRF) is always detectable without chemical pre-treatment (*i.e.* fluorophore addition), has minimal matrix effects, detects both bound and free metal ions in the cell, and is readily detected for most biologically relevant metals.

With the development of intense, third-generation synchrotron sources, XRF imaging of intact cells using either dried or cryogenically frozen samples has become a widely used technique. Recent work (Wang *et al.*, 2014) used raster scanning of air-dried cells in fly scan mode with unsupervised cell identification to separate cell types and quantify the elemental content of individual cells from XRF datasets. This work successfully identified hundreds of cells using imaging techniques. However, imaging techniques do not permit easy time-dependent manipulations of cells, and are not readily accessible to other techniques (*e.g.* light scattering, fluorescence cell sorting) which have been optimized for intact fluid cells. The combination of cytometry, which allows the manipulation of single cells in biologically relevant fluids with XRF for elemental analysis offers a solution to the need for single-cell metallome analysis. A brief report (Sophie-Charlotte *et al.*, 2013) noted construction of an XRF cytometer using a syringe pump and a microfluidic channel but did not describe any characterization of the device. In this paper, we describe the development and testing of an XRF-based flow cytometer that permits detection of total trace element levels in aqated, living, actively respiring cells with moderate throughput.

2. Design

Our design goal was an XRF flow cytometer that could sample individual cells with a per-cell measurement time of ~ 1 s. This relatively slow rate is a result of the need to acquire appropriate counting statistics using current synchrotron sources. At this rate, the jet flow and hydrodynamic focusing used in conventional cytometers are not possible. Rather, we relied on simple fluid flow through a capillary, with the capillary diameter the sole constraint on cell position.

A schematic illustration of the instrument is shown in Fig. 1. There are two visible-light cameras to allow determination of cell position. The two nearly perpendicular cameras allowed us to determine cell position in three dimensions and thus

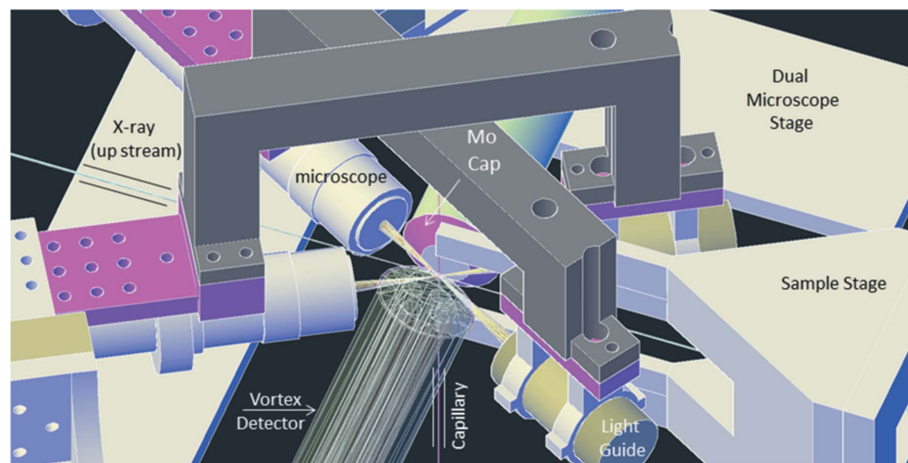


Figure 1 Instrument design. Schematic illustration of the instrument showing the two horizontal microscopes, the sample holder and the XRF detectors.

correct for beam inhomogeneity (see below); some early measurements used only a single camera and were thus only semi-quantitative. Two X-ray fluorescence detectors, each equipped with a Mo collimator to decrease detected scatter (Behne *et al.*, 2001), are aligned perpendicular to the beam direction. The distance between the detectors was 2.8 cm giving a 1.4 sample-to-detector distance, although some early tests used a larger sample-to-detector distance (~ 2.5 cm).

Hydrophilic capillaries [PMMA, polymethylmethacrylate; 50 μm inner diameter (i.d.), 100 μm outer diameter (o.d.)] were loaded using capillary action. The linear velocity while filling was $\sim 1 \text{ mm s}^{-1}$ so that a 20 cm capillary took ~ 10 min to fill. A water droplet was used to trap an air pocket at the end of the capillary in order to slow the linear velocity to $\sim 5 \mu\text{m s}^{-1}$. Hydrophobic capillaries were filled using a syringe and the flow was controlled by adjusting the relative height (Δh) of the reservoir on each end. This syphon pump allowed precise control of cell velocity (see Fig. S1 of the supporting information); each 1 μm difference in Δh increased the linear velocity by $\sim 0.3 \mu\text{m s}^{-1}$ (25 μm i.d. capillaries) or $\sim 1.4 \mu\text{m s}^{-1}$ (50 μm i.d.).

3. Conceptual approach to analysis

3.1. Combining XRF and video data sets

Cells have variable sizes, metal content, velocities and in some cases overlapping beam residence times, making single cell quantification of metal content impossible from the measured XRF alone. In order to deconvolve the signals from cells, one needs to know the path of each cell through the beam at every point in time. With conventional cytometry, this is accomplished using light scattering. Since there was not sufficient X-ray scattering contrast between capillary+solution and capillary+solution+cell to allow cell detection, we instead used visible-light microscopy. Video data were collected synchronously with XRF using a visible-light microscope (Mitutoyo, M Plan Apo 5 \times /10 \times objective; Infinitube Standard with Iris diaphragm; Edmund Optics 5012C, Color GigE Camera). Although the identification and tracking of objects in video data and the fitting of XRF data are well established (Herrero & Bescós, 2009), we are not aware of previous efforts to combine XRF time traces with cellular ‘tracks’ to deconvolve single-cell total integrated fluorescence counts.

To align the video and XRF data, we first estimated the beam location in the video. As the beam irradiates the capillary it also slowly (5–10 min) discolors it, providing a visual estimate of beam position. Each frame of the video was converted into a binary mask identifying the position and area of each cell in that frame. The xy coordinates of each cell were then connected across frames based on minimizing changes in cell size and frame-to-frame cell displacement. The vertical profile of the beam (see §4.2) was initially aligned with the capillary beam image. Convolution of each cell’s profile with the beam profile, followed by column normalization to unity, gave an $M \times N$ matrix, \mathbf{A} , of theoretical fluorescence traces,

where M is the XRF scan number (proportional to time) and N is the cell number. This gives the predicted fluorescence if each cell had the same composition. Interpolation of the array’s time frame onto the time frame of the XRF data and deconvolution of the amplitudes for each column allows the total integrated counts of each cell to be calculated using the entirety of the dataset.

If \mathbf{F} is the XRF time trace for a given element, then

$$\mathbf{F} = \mathbf{A}\mathbf{c}, \quad (1)$$

where \mathbf{A} is the $M \times N$ array above and \mathbf{c} is the amount of that element in each cell. In principle, analysis requires only that equation (1) be solved for \mathbf{c} . In practice, \mathbf{A} depends both on the slope (differences in frame rate) and intercept (differences in t_0) that are used to align the video and XRF time bases, and on the spatial alignment of the measured beam profile on the video frame. Therefore, the time base and beam position (a vertical shift and rotation of the capillary relative to the video frame) were first refined iteratively to minimize the mean-squared difference between the predicted and observed XRF for the element with the largest signal, and these values were then used for the other elements.

3.2. Integrating with respect to position

Matrix \mathbf{c} in equation (1) has units of normalized counts s^{-1} which, with appropriate calibration (see §4.3), can be converted to fg s^{-1} . This would give cellular mass if each cell had a constant velocity and spent the same amount of time in the beam. Since this is not the case, data were converted from time domain to space domain using the measured frame-by-frame vertical position (y) of each cell. The y -coordinates were sorted in increasing order and the corresponding x -coordinates and counts, \mathbf{c} , were reorganized to match. By interpolating these data onto a uniform y -grid we obtained a new curve that is equivalent to the counts corresponding to convolution of the beam profile with the cell composition. Integration of this curve gives the total metal composition of the cell.

4. Experimental

4.1. Sample preparation and handling

Trypsinized bovine red blood cells (bRBCs, 0.1 hematocrit, obtained from Lampire) were diluted 1:20–30 using phosphate buffered saline (PBS; Fisher Scientific) depending on capillary size. The stock and the diluted aliquots were kept at 4°C. NIH3T3 cells were grown from cryopreserved aliquots in atmospheric O_2 and 5% CO_2 at 37°C. Cells were thawed and placed in 12 ml of complete medium (CM) [Dulbecco’s modified Eagle medium, high glucose variant (4.5 mg ml^{-1}), supplemented with 10% donor bovine serum] in 75 cm^2 flasks at 5×10^5 cells flask^{-1} (6.7×10^3 cells cm^{-2}). The cells were fed on day 2 (75% replacement) and then subcultured on day 5 into six 75 cm^2 flasks at 5.5×10^5 cells flask^{-1} . After two days of further proliferation, the cells were subcultured into twelve 75 cm^2 flasks at 5.5×10^5 cells flask^{-1} . The next day CM

medium in flasks was increased from 12 ml to 200 ml. This CM medium increase promotes cell survival outside the incubator at room temperature and atmospheric CO₂ levels for about a week. Cells were transported to the Advanced Photon Source (APS) and kept at room temperature and atmospheric CO₂ for 3–5 days. Cells were then harvested and resuspended in PBS solution for measurement of metal concentration. Yeast experiments were performed using the *Saccharomyces cerevisiae* yeast strain BY4741, grown in YPD rich media at 30°C overnight. Cells were transported to the APS in YPD media, stored at 4°C and washed with PBS prior to measurement.

4.2. Beamline parameters

Experiments were performed using the Bio-CAT (Sector 18) and 20-ID-B beamlines available at the APS. Data were measured using both hydrophilic (PMMA) and hydrophobic (Zeonor[®]) capillaries and with two sizes of capillary: i.d. 50 µm, o.d. 100 µm and i.d. 25 µm, o.d. 50 µm. Each position of a capillary was scanned for 5–10 min while the XRF signal was captured at 4 Hz using an energy-resolving solid state detector (Vortex-ME4; SII NanoTechnology). A typical scan detected between 20 and 60 cells, depending on the cell density. After each scan, the capillary was translated by 100 µm vertically to avoid excessive radiation damage to the capillary.

The incident beam energy (13 keV) was selected using a Si(111) monochromator and gave a total incident flux of $\sim 10^{12}$ photons s⁻¹. Using a pair of Kirkpatrick–Baez mirrors, the beam was focused to 50 µm horizontal \times 20 µm vertical (FWHM) for the larger capillaries and 25 µm horizontal \times 6 µm vertical for the smaller capillaries. The beam profile was measured by a knife-edge scan. Fluorescence counts were normalized to the incident intensity measured with a N₂-filled ion chamber immediately upstream from the sample.

4.3. Instrument calibration

The instrument was calibrated using standard solutions [~ 100 , ~ 200 and ~ 500 µM Cr(NO₃)₃, Fe(NO₃)₃, Ni(NO₃)₂ in water] with concentrations confirmed by ICP-OES (Perkin-Elmer Optima 2000 DV with Winlab software) pre- and post-experiment. Due to lack of a calibration and the need to extrapolate, reported values for *K* are only semi-quantitative.

Prior to collecting XRF data for each standard, a blank scan of each capillary was obtained. The capillary was then filled with the standard solutions and the XRF spectra were measured. The blank-subtracted data were then fitted with a series of Gaussians, one for each *K*α and *K*β peak; the summation of the area under the *K*α and *K*β curves was taken as the fluorescence counts for each element. Instrument sensitivity (counts fg⁻¹ s⁻¹ I₀⁻¹) for each element was determined from the slope of the calibration curves and, as expected, increased with increasing atomic number. The optimized parameters from the standards (energy calibration and Gaussian peak widths) and *K*α:*K*β branching ratios were held constant in subsequent linear least-squares fits of the XRF data for the cytometer traces.

4.4. XRF fitting

XRF data were fit using the *M-BLANK* program (Crawford, 2015). A blank was calculated using data from time points at which no cells were present in the beam, and was then subtracted from the data. The blank-subtracted XRF for each time point was then fit in a linear least-squares sense using a series of Gaussians with the energy calibration, Gaussian widths and *K*α:*K*β ratios fixed at the experimentally determined reference values.

5. Results

5.1. Initial measurements using PMMA capillaries

Using hydrophilic PMMA capillaries (50 µm i.d., 100 µm o.d.), a total of 805 bRBC cells were detected in 24 individual scans taken over a time period of ~ 5 h. In order to avoid detector saturation due to scattering from these relatively large capillaries, the sample-to-detector distance was increased to 2.5 cm. Measurements were made with a linear velocity of $3.2 \mu\text{m s}^{-1} \pm 2.5 \mu\text{m s}^{-1}$ which resulted in cells being exposed to the beam for a mean of ~ 5 s. A total of 31 mouse fibroblasts (NIH3T3) cells were detected in six individual scans taken over a time period of ~ 4 h. The data were measured with a higher linear velocity ($8.3 \mu\text{m s}^{-1} \pm 5.4 \mu\text{m s}^{-1}$) such that, although 3T3 cells are larger than bRBC cells, the mean exposure time in the beam (~ 5.5 s) was almost the same.

From these measurements, the XRF spectrum for a single bRBC (not shown) had an Fe fluorescence peak that was detectable, albeit with high uncertainty; there was no Zn peak that was detectable above the noise level. Across all of the cells, the average Fe content was 58 ± 27 fg cell⁻¹. Assuming an average cell volume of 80 fL, this gives an apparent Fe concentration of ~ 13 mM, in reasonable agreement with expectation. For 3T3 cells, Zn and K fluorescence peaks were both detectable above the background noise but once again Fe was undetectable in individual XRF traces. The average apparent cellular masses for Zn and K were 27 ± 16 fg cell⁻¹ and 789 ± 550 fg cell⁻¹, respectively. Assuming a 3T3 cell volume of 4 pL, these give apparent concentrations of 100 µM Zn and 6 mM K. The former is, once again, in reasonable agreement with expectation, while the latter is much lower than the expected value of ~ 150 mM. This most likely reflects the significant absorption of potassium *K*α X-rays by the buffer and the capillary, and the lack of a calibration standard for potassium. Histograms summarizing the apparent Fe content of bRBCs, and the apparent Zn and K content of fibroblasts are shown in Fig. S2. Also shown is a correlation plot summarizing the relationship between Zn and K in fibroblasts.

5.2. Capillary contaminants

The PMMA capillaries that were used in the initial measurements showed significant impurities. In an effort to decrease contamination, we explored a variety of capillary materials (see Fig. S3). All of the capillaries that we tested

showed non-negligible levels of Fe, K, Zn and Cu contaminants, with hydrophobic capillaries (Zeonor[®] and Zeonex[®]) containing the lowest levels. We ultimately switched to Zeonor[®] due to relatively lower levels of contaminants. In addition to reducing the level of background contaminants, these capillaries had a smaller diameter, thus decreasing the scatter and allowing a smaller sample-to-detector distance.

The importance of background contamination for detection limits and sensitivity is illustrated by Fig. 2, which shows a comparison between the XRF spectrum for the average of all 805 bRBC cells measured using PMMA capillaries (top) and the XRF spectrum for the average of bRBC 73 cells measured using hydrophobic capillaries (middle). In the former, only the Fe $K\alpha$ and Fe $K\beta$ peaks are detectable, and there is noticeable noise even in these. In the latter, Fe, S, K and possibly Zn peaks are detectable, and the noise level is noticeably lower, despite the fact that this is the average of one-tenth as many cells. In part, the lower noise is due to the smaller sample-to-detector distance (1.4 *versus* 2.5 cm) that was made possible by the smaller capillary; the smaller distance should give an approximately three-fold increase in count rate. However, we attribute most of the improvement to the significant decrease in background contamination.

5.3. Measurements using hydrophobic capillaries

Using hydrophobic Zeonor[®] capillaries (25 μm i.d.) we were able to see signals from individual cells. Fig. 3 shows the

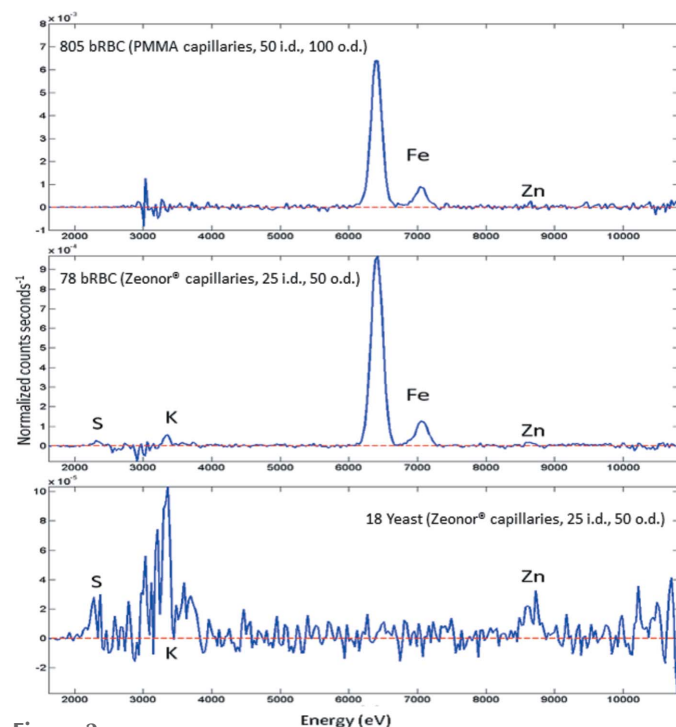


Figure 2
Average XRF spectra. The average of the XRF spectrum for 805 bRBCs measured with a 50 μm i.d. hydrophilic capillary (top), 78 bRBCs measured with a 25 μm i.d. hydrophobic capillary (middle), and 18 yeast cells measured with a 25 μm i.d. hydrophobic capillary (bottom). Spectra for all time points were processed as described in the text to remove the capillary background and the time points representing those times when cells were in the beam were then averaged to give these spectra.

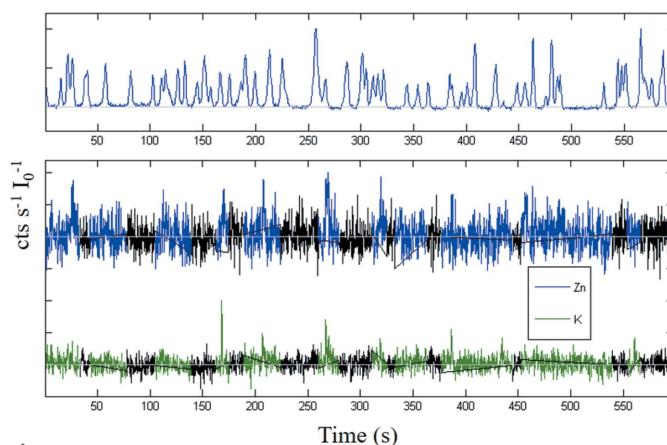


Figure 3
Time scans. Representative time-scans for the Fe channel for bRBC (top) and for the Zn and K channels for yeast (bottom). The y-axis has been normalized to an absolute negative intensity of 1. For yeast, Zn has been vertically shifted for visualization. The black lines for both Zn and K in the yeast traces correspond to time points when no cells were in the beam. The light gray lines on all three traces mark the zero in the background-subtracted data.

fitted time course for the Fe signal in bRBCs as well as the K and Zn signals in yeast. For bRBCs, it is clear that the signal is detectable well above the background. Although for these yeast measurements there is no obvious Zn or K signal in the time trace above the background noise level, it is nevertheless the case that these elements *are* detectable in the average XRF spectrum (Fig. 2). Relatively straightforward improvements, such as addition of a He shroud to decrease background scatter or use of a slower flow rate to increase cell residence time, should render these elements detectable in single cells.

A total of 12 scans, ranging from 5 to 10 minutes each, were made on bRBC samples detecting a total of 131 bRBCs. At the highest cell densities, we were able to interrogate 73 cells in a single 10 min scan. The apparent mass of Fe in these cells was $48.8 \pm 19.9 \text{ fg cell}^{-1}$, comparable with the data collected using hydrophilic capillaries. Using the same protocol to fit the Zn peaks gave an apparent Zn composition of $\sim 0.4 \text{ fg cell}^{-1}$.

Using the higher-sensitivity hydrophobic capillaries we were able to make preliminary measurements on 18 yeast cells, which are much smaller than 3T3 cells and lack the high Fe concentration of bRBC cells. Although only preliminary, these data (Fig. 2, bottom) show the potential of the instrument. There are detectable peaks for S, Zn and K. The Zn peak represents a mean cellular content of $\sim 0.6 \text{ fg cell}^{-1}$ or, assuming a cell volume of 50 fL, a concentration of $\sim 180 \mu\text{M}$, in reasonable agreement with expectations. The apparent amounts of S and K (0.6 and 37 fg cell^{-1} , respectively) are likely to be significantly underestimated, due to significant absorption at these low fluorescence energies.

6. Tests for accuracy

In order to test the accuracy of our data analyses, we examined the effect of background contamination, cell velocity, the

horizontal variability of the beam, and cell density on the apparent Fe content.

6.1. Background Fe contamination

In order to test whether variations in the capillary background interfered with cellular quantitation we determined the apparent mean Fe content from 24 different scans, each representing ~20 to 60 cells, each measured at a different capillary location. The apparent mean Fe content is compared with the measured Fe background in Fig. S4. There is no discernible dependence of apparent Fe content on background despite a 50-fold variation in Fe background level for different portions of the capillary. Both the lowest and highest mean Fe masses are found for scans with among the lowest contamination. In contrast with the mean, the standard deviation of the apparent Fe content does show a dependence on background, increasing as the background increases.

6.2. Cell velocity and mass quantitation

Depending on the details of capillary conditions there was a ~10-fold variation in cell velocity during measurement. If not properly accounted for in our analysis, this could affect the apparent XRF-determined masses. A plot of calculated Fe content as a function of cellular velocity through the beam shows no dependence of the apparent Fe content on cell velocity (see Fig. S5).

6.3. Horizontal beam profile

Since the beam intensity is not completely uniform horizontally, the measured fluorescence will vary slightly depending on the *x*-coordinate of a cell at the time that it

passes through the beam. This is illustrated in Fig. 4, where the apparent Fe content is plotted as a function of the *x*-coordinate of each cell. If all of the cells contained the same amount of Fe, the measured Fe content should reproduce the measured horizontal beam profile. In fact, the beam profile can be scaled vertically (see Fig. 4) to align with data. Using this profile, we can calculate the relative signal that should be seen for different horizontal cell positions. At the peak, a cell will have an intensity that is ~1.4-fold larger than the average for the capillary, while, at the edge, the intensity will be approximately two-thirds as large as at the average for the capillary. The apparent Fe content after correcting for horizontal cell position is shown in Fig. 4(b). The cells still show significant variability in Fe content, demonstrating that the variability is not an artefact of horizontal beam heterogeneity. However, the histogram before correction (Fig. 4c) appears to be slightly less symmetric than the histogram after correction (Fig. 4d).

6.4. Cell density

For some scans, the cellular concentration was high enough that two or more cells were in the beam at the same time. In order to test whether we were able to reliably deconvolve these signals we compared the apparent distributions for overlapping *versus* non-overlapping cells (see Fig. S6) from early measurements. The results for one or two cells are the same, but if three or more cells are in the beam the standard deviation in apparent mass increases, suggesting that the fitting algorithm failed to correctly assign fluorescence to each cell. For this reason, subsequent data were measured at lower cell density in order to minimize overlaps and these initial data were culled to remove all instances with three or more cells in the beam.

It is worth noting that some of the variation that we attributed to cell-cell overlap could in fact be due to variations in horizontal position. These early data were measured with only a single camera and consequently the horizontal position could not be determined. If crowding tended to push cells away from the center of the capillary, where the beam is most intense, and towards the sides, where it is less intense, this movement alone could account for some, and perhaps all, of the increase seen in Fig. S6. If so, the use of two cameras for full three-dimensional position determination may permit the use of higher cell densities. This is a subject for future investigation.

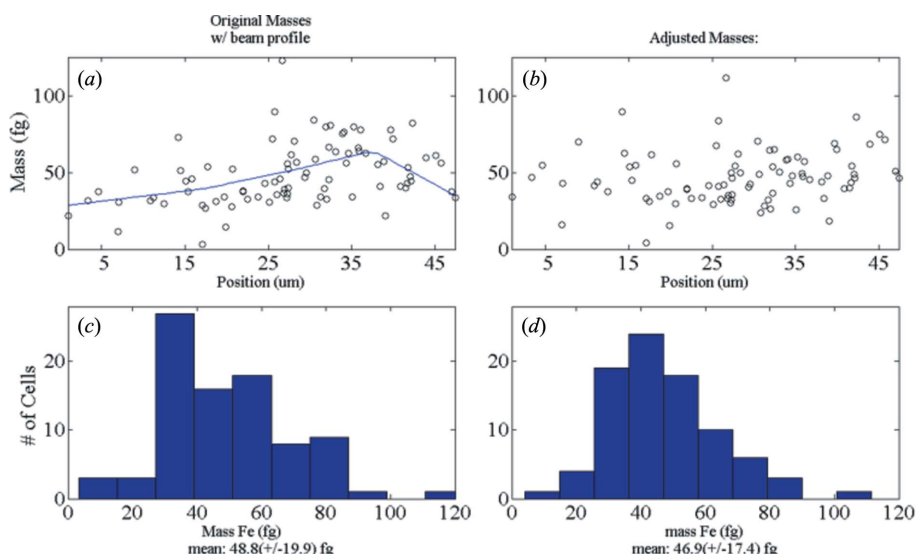


Figure 4 Effect of horizontal position on apparent Fe content. (a) Apparent Fe content *versus* *x*-coordinate of the cell when crossing the beam. The left wall of the capillary defines 0 μm . The experimental horizontal beam profile was scaled vertically to give the best overlap with measured masses (blue line). (b) Data after correction for horizontal intensity variation. Histogram of apparent Fe content before (c) and after (d) correction.

7. Discussion

The experimentally determined mean Fe content for individual bRBCs,

~ 50 fg, is in good agreement with previous findings (Herring *et al.*, 1960a; Kakkar & Makkar, 2009; Shamberger, 2003). Although the data are significantly noisier, the average Zn content (~ 0.4 fg cell $^{-1}$) is again in good agreement with previous measurements (Herring *et al.*, 1960a; Wang *et al.*, 2014). Even with these noisy data, we can see the importance of single-cell measurements: the distribution of Fe is much larger than would be expected simply from experimental uncertainty. Under our conditions, an average bRBC traveling at the average velocity gives ~ 173 fluorescent counts and ~ 20 background counts for Fe while passing through the beam, corresponding to a statistical uncertainty of $\sim \sqrt{193}/173 = 8.0\%$ or ~ 4.7 fg. The observed standard deviation (~ 20 fg) is ~ 4 -fold larger, suggesting that the observed distribution is dominated by biological variability not experimental uncertainty. In principle, variations in cell size might account for some of this variability. However, a plot of mass *versus* cell radius shows no apparent correlation (Fig. 5) suggesting that the observed distribution may be a biologically relevant distribution, perhaps reflecting, for example, variations in Fe content as a function of cell age.

Although the data are quite noisy in comparison with the bRBC Fe data, the experimentally determined Zn content of individual NIH3T3 mouse fibroblasts is in good agreement with known mammalian concentrations (Eide, 2006). As with the bRBC Fe content, the measured distribution appears to be wider than would be expected simply from counting statistics. Although there is clearly a K signal from 3T3 cells, the lack of a calibration standard prevents accurate quantitation at this time.

In addition to the data collected for the bRBCs and mouse fibroblasts, we were also able to measure preliminary composition data for yeast. These are much more challenging than the high-iron-content bRBC cells or the large NIH3T3 cells. Our preliminary results demonstrate that, with a realistic increase in signal-to-noise ratio from addition of a He shroud

and/or slower cell transit time, even these cells should be accessible. In our design, we opted for the ease of sample handling that comes with a single capillary. However, it may be possible to optimize the system even further if the scattering background were minimized by building in Si₃N₄ windows, as done recently for X-ray scattering studies of living cells (Weinhausen & Köster, 2013).

Our ultimate goal was to measure complete XRF spectra for single cells. Although we have not yet fully achieved this goal, our sensitivity is sufficient to give XRF spectra showing Fe and K from single bRBCs, Zn from single 3T3 cells, as well as K and Zn in single yeast cells, as shown in Fig. 6. Based on counting statistics and a minimum signal-to-noise ratio of 1, our estimated single-cell detection limits are ~ 7 fg for Fe and ~ 2.3 fg for Zn. Our inability to see Zn in single bRBC or Fe in yeast reflects the fact that these are, in both cases, below our current detection limits.

8. Conclusions

We have successfully demonstrated the implementation of an XRF flow cytometer capable of measuring XRF spectra for individual cells. With realistic improvements in signal size it should be possible to determine the complete metallome for individual cells. Even with these initial data, it is clear that single-cell measurements provide significantly more information about metal composition than can be obtained from bulk compositional analysis.

Acknowledgements

This research was funded in part by the National Science Foundation under (NSF-IDBR-0852802 to JEPH). LD was supported by the National Institutes of Health (9 P41 GM103622). This research used resources of the Advanced Photon Source, a US Department of Energy (DOE) Office of Science User Facility operated for the DOE Office of Science by Argonne National Laboratory under Contract No. DE-AC02-06CH11357. Sector 20 facilities at the APS is supported by the US Department of Energy, Basic Energy Sciences, the Canadian Light Source and its funding partners, the University of Washington, and the Advanced Photon Source. The staff of the LSA Scientific Instruments Shop provided valuable collaboration on sample holder design. The authors would like to thank Erik Guetschow for assistance with the syphon pump.

References

- Ariño, J., Ramos, J. & Sychrová, H. (2010). *Microbiol. Mol. Biol. Rev.* **74**, 95–120.
- Behne, E. A., Feng, Y. & Seidler, G. T. (2001). *Rev. Sci. Instrum.* **72**, 3908–3913.

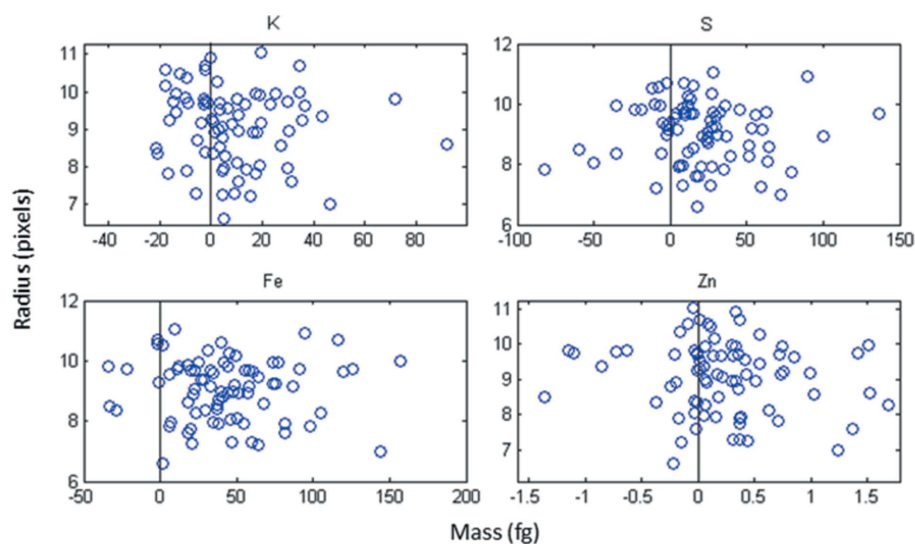


Figure 5
Cell radii *versus* mass. The fitted mass of K, S, Fe and Zn in each cell from a single scan of bRBCs *versus* cell radius as measured using the optical microscopes.

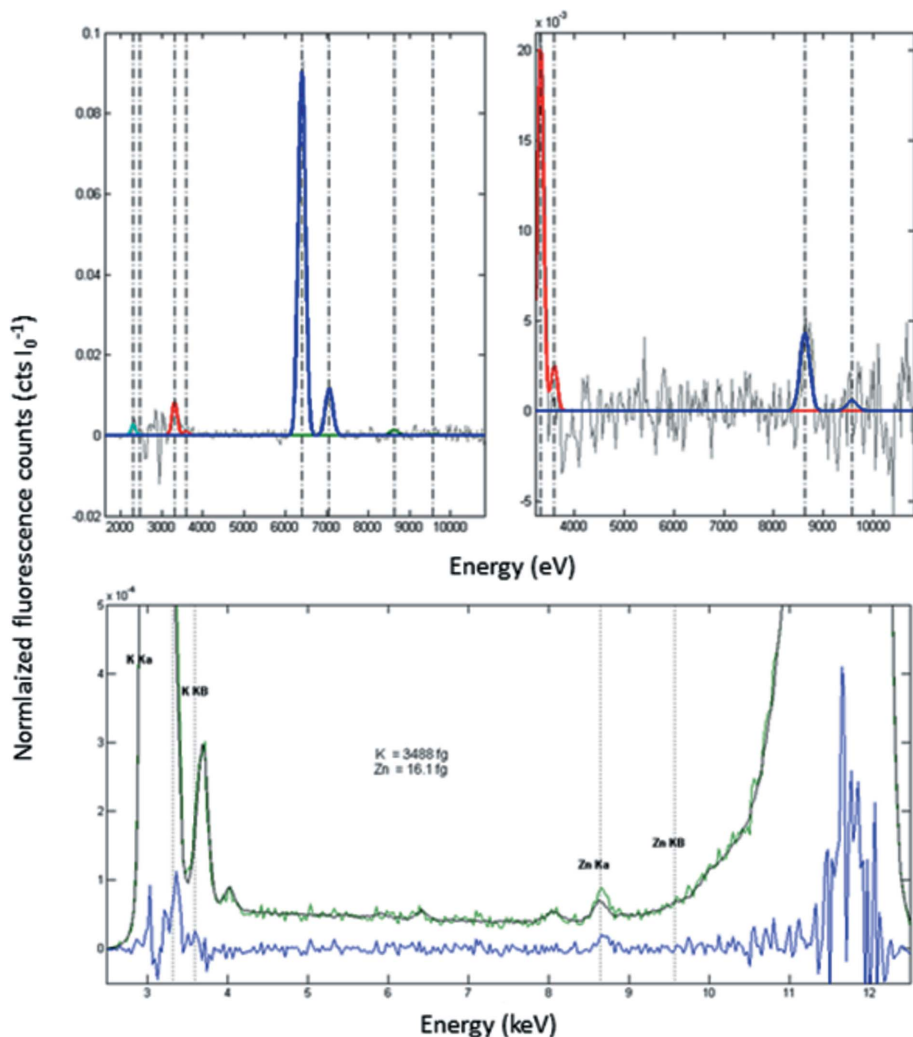


Figure 6
Single-cell spectra. XRF data for single cells of bRBC (top left), yeast (top right) and 3T3 (bottom). For the bRBC and yeast spectra, the background-subtracted cell spectrum is shown in gray. For the bRBC cell the fitted peaks for S, K, Fe and Zn are shown in cyan, red, blue and green, respectively; for yeast, the fitted peaks for K and Zn are shown in red and blue, respectively. The 3T3 data (bottom) were measured with a 50 μm i.d. hydrophilic capillary and thus have worse signal-to-noise ratio in comparison with the other data, which were measured using 25 μm i.d. hydrophobic capillaries. For the 3T3 cell, the green and gray lines show the total XRF and the capillary blank, respectively; the blank-corrected XRF is shown in blue, with the energies of the K and Zn fluorescence lines indicated by vertical dashed lines. No fits are shown for the 3T3 cell.

Bertinato, J. & L'Abbé, M. R. (2004). *J. Nutr. Biochem.* **15**, 316–322.
 Brehm-Stecher, B. F. & Johnson, E. A. (2004). *Microbiol. Mol. Biol. Rev.* **68**, 538–559.
 Chillappagari, S., Seubert, A., Trip, H., Kuipers, O. P., Marahiel, M. A. & Miethke, M. (2010). *J. Bacteriol.* **192**, 2512–2524.
 Crawford, A. (2015). PhD thesis, University of Michigan, USA.
 Dann, C. E., Wakeman, C. A., Sieling, C. L., Baker, S. C., Irnov, I. & Winkler, W. C. (2007). *Cell*, **130**, 878–892.
 Davey, H. M. & Kell, D. B. (1996). *Microbiol. Rev.* **60**, 641–696.
 Dlouhy, A. C. & Outten, C. E. (2013). *Metal Ions in Life Sciences*, Vol. 12, *Metallomics and the Cell*, edited by L. Banci, pp. 241–278. Dordrecht: Springer.
 Eide, D. J. (2006). *Biochim. Biophys. Acta*, **1763**, 711–722.
 Eide, D. J. (2009). *J. Biol. Chem.* **284**, 18565–18569.

Fahrni, C. J. (2007). *Curr. Opin. Chem. Biol.* **11**, 121–127.
 Groombridge, A. S., Miyashita, S., Fujii, S., Nagasawa, K., Okahashi, T., Ohata, M., Umemura, T., Takatsu, A., Inagaki, K. & Chiba, K. (2013). *Anal. Sci.* **29**, 597–603.
 Hartwig, A. (2001). *Antioxid. Redox Signal.* **3**, 626–634.
 Herrero, S. & Bescós, J. (2009). *Background Subtraction Techniques: Systematic Evaluation and Comparative Analysis*. Berlin/Heidelberg: Springer.
 Herring, W. B., Leavell, B. S., Paixo, L. M. & Yoe, J. H. (1960a). *Am. J. Clin. Nutr.* **8**, 846–854.
 Herring, W. B., Leavell, B. S., Paixao, L. M. & Yoe, J. H. (1960b). *Am. J. Clin. Nutr.* **8**, 855–863.
 Ho, K.-S. & Chan, W.-T. (2010). *J. Anal. At. Spectrom.* **25**, 1114–1122.
 Kakkar, N. & Makkar, M. (2009). *Lab. Med.* **40**, 549–555.
 Kalisky, T. & Quake, S. R. (2011). *Nat. Methods*, **8**, 311–314.
 Kamizono, A., Nishizawa, M., Teranishi, Y., Murata, K. & Kimura, A. (1989). *Mol. Gen. Genet.* **219**, 161–167.
 Kikuchi, K., Komatsu, K. & Nagano, T. (2004). *Curr. Opin. Chem. Biol.* **8**, 182–191.
 Leslie, M. (2011). *Science*, **331**, 24–26.
 Li, L. T. & Kaplan, J. (1998). *J. Biol. Chem.* **273**, 22181–22187.
 Madsen, E. & Gitlin, J. D. (2007). *Annu. Rev. Neurosci.* **30**, 317–337.
 McRae, R., Bagchi, P., Sumalekshmy, S. & Fahrni, C. J. (2009). *Chem. Rev.* **109**, 4780–4827.
 Miyashita, S., Groombridge, A. S., Fujii, S., Takatsu, A., Chiba, K. & Inagaki, K. (2014). *Anal. Sci.* **30**, 219–224.
 Mueller, L., Traub, H., Jakubowski, N., Drescher, D., Baranov, V. I. & Kneipp, J. (2014). *Anal. Bioanal. Chem.* **406**, 6963–6977.
 Musat, N., Halm, H., Winterholler, B., Hoppe, P., Peduzzi, S., Hillion, F., Horreard, F., Amann, R., Jorgensen, B. B. & Kuypers, M. M. M. (2008). *Proc. Natl Acad. Sci. USA*, **105**, 17861–17866.
 Pagani, M. A., Casamayor, A., Serrano, R., Atrian, S. & Ariño, J. (2007). *Mol. Microbiol.* **65**, 521–537.
 Penner-Hahn, J. E. (2014). *Metallomics and the Cell*, Vol. 12, edited by L. Banci. Dordrecht: Springer.
 Shamberger, R. J. (2003). *Biol. Trace Elem. Res.* **94**, 123–129.
 Sophie-Charlotte, G., Britta, W., Sarah, K., Jesse, W., David, V., Lydia, F. & Stefan, V. (2013). *J. Phys. Conf. Ser.* **463**, 012005.
 Wang, S., Ward, J., Leyffer, S., Wild, S. M., Jacobsen, C. & Vogt, S. (2014). *J. Synchrotron Rad.* **21**, 568–579.
 Weinhausen, B. & Köster, S. (2013). *Lab Chip*, **13**, 212–215.
 Yang, L. C., McRae, R., Henary, M. M., Patel, R., Lai, B., Vogt, S. & Fahrni, C. J. (2005). *Proc. Natl Acad. Sci.* **102**, 11179–11184.
 Zhao, H., Butler, E., Rodgers, J., Spizzo, T., Duesterhoeft, S. & Eide, D. (1998). *J. Biol. Chem.* **273**, 28713–28720.